

Flat rotation curves and low velocity dispersions in KMOS star-forming galaxies at $z \sim 1$ [★]

E. M. Di Teodoro^{1,2}, F. Fraternali^{1,3}, and S. H. Miller⁴

¹ Department of Physics and Astronomy, University of Bologna, 6/2 Viale Berti Pichat, 40127 Bologna, Italy

² Research School of Astronomy and Astrophysics – The Australian National University, Canberra, ACT, 2611, Australia
e-mail: edi.teo@mso.anu.edu.au

³ Kapteyn Astronomical Institute, Postbus 800, 9700 AV Groningen, The Netherlands

⁴ University of California – Irvine, Irvine, CA 92697, USA

Received 15 February 2016 / Accepted 18 July 2016

ABSTRACT

The study of the evolution of star-forming galaxies requires the determination of accurate kinematics and scaling relations out to high redshift. In this paper we select a sample of 18 galaxies at $z \sim 1$, observed in the H α emission line with KMOS, to derive accurate kinematics using a novel 3D analysis technique. We use the new code ^{3D}BAROLO, which models the galaxy emission directly in 3D observational space, without the need to extract kinematic maps. This major advantage of this technique is that it is not affected by beam smearing and thus it enables the determination of rotation velocity and intrinsic velocity dispersion, even at low spatial resolution. We find that (1) the rotation curves of these $z \sim 1$ galaxies rise very steeply within few kiloparsecs and remain flat out to the outermost radius and (2) the H α velocity dispersions are low, ranging from 15 to 40 km s⁻¹, which leads to $V/\sigma = 3$ –10. These characteristics are similar to those of disc galaxies in the local Universe. Finally, we also report no significant evolution of the stellar-mass Tully-Fisher relation. Our results show that disc galaxies are kinematically mature and rotation-dominated at $z \sim 1$ already.

Key words. galaxies: evolution – galaxies: high-redshift – galaxies: kinematics and dynamics

1. Introduction

In the last decade the advent of integral field spectroscopy (IFS) has remarkably widened our possibilities of investigating the physical properties of galaxies in the high-redshift Universe. Several surveys have taken advantage of the new generation of integral field units (IFUs), such as the SINS/zC-SINF (Förster Schreiber et al. 2009) and MASSIV (Contini et al. 2012) surveys with the Spectrograph for INtegral Field Observations in the Near Infrared (SINFONI, Eisenhauer et al. 2003), the OSIRIS survey (Law et al. 2007, 2009) with Keck/OSIRIS (Larkin et al. 2006), KMOS^{3D} (Wisnioski et al. 2015) and KROSS (Stott et al. 2016) with the *K*-band Multi-Object Spectrograph (KMOS; Sharples et al. 2013). These surveys have observed high- z star-forming galaxies and mapped their kinematics through optical/near-infrared emission lines, such as H α , nitrogen and oxygen lines, tracing the ionized phase of warm gas and ongoing star formation.

Spatially resolved information on the kinematics and dynamics of high- z systems can provide new insights to draw the evolutionary picture of galaxies in the epoch near the peak of cosmic star formation rate (SFR) at $z \sim 1$ –3. In this epoch, the baryonic mass assembly was likely regulated by the equilibrium between the gas accretion from the intergalactic medium (IGM) or mergers and the stellar/AGN feedback (e.g. Dekel et al. 2009; Dutton et al. 2010; Lilly et al. 2013). The relation between SFR and stellar mass (M_*), the so-called *main-sequence* (MS) of galaxies (e.g. Elbaz et al. 2011; Speagle et al. 2014), supports

the scenario of a relatively smooth growth of galaxies in disc-like structures with respect to bursts of star formation driven by merger episodes (e.g. Rodighiero et al. 2011). The in situ growth rapidly ceases at $M_* > 10^{11} M_\odot$ and above this stellar mass galaxies already appear quenched at $z \sim 2.5$ (e.g. Whitaker et al. 2012). In this context, the study of the kinematics of high- z galaxies can supply unique information on the internal dynamical state of these systems, for instance, revealing the signs of merger-driven or secular mass growths.

Kinematic studies through IFS revealed that the majority of star-forming galaxies in the stellar mass range $10^9 < M_*/M_\odot < 10^{11}$ at $z > 1$ are disc-like systems (e.g. Förster Schreiber et al. 2009; Genzel et al. 2008; Epinat et al. 2009, 2012; Tacchella et al. 2015), with an actual fraction of rotating discs shifting from an initial estimate of 30% (Genzel et al. 2006; Förster Schreiber et al. 2006) to 80–90% (Wisnioski et al. 2015). These star-forming disk galaxies are rotationally supported with circular velocities of 100–300 km s⁻¹ already a few Gyr after the Big Bang (e.g. Cresci et al. 2009, Gnerucci et al. 2011). The predominance of disc-like kinematics over irregular or dispersion-dominated kinematics seems to be in favour of a smooth mass growth of galaxies. However, the measured H α velocity dispersions in these systems are of the order of 50–100 km s⁻¹ (Glazebrook 2013), which is a factor 2–4 higher than the values found in local spiral galaxies (Bershady et al. 2010; Epinat et al. 2010); this suggests that discs at high redshift are morphologically and dynamically different from local ones. The general picture is that young discs were much more turbulent in the past and then they evolved towards a cooler dynamical state with a V/σ increasing with the cosmic time.

[★] The reduced datacubes as FITS files are only available at the CDS via anonymous ftp to cdsarc.u-strasbg.fr (130.79.128.5) or via <http://cdsarc.u-strasbg.fr/viz-bin/qcat?J/A+A/594/A77>

The kinematics is also used to study the evolution of the scaling relations throughout cosmic time, in particular the Tully-Fisher relation (TFR; Tully & Fisher 1977), which correlates the rotation velocity (hence the dynamical mass) to the disc luminosity (or the stellar mass). The evolution of TFR is related to how disc galaxies assembled. The stellar mass TFR (i.e. M_* versus V_{rot}) at low redshift is well constrained (e.g. Bell & de Jong 2001; McGaugh 2005; Meyer et al. 2008), but at intermediate-high redshifts the derived relations have larger scatter (Conselice et al. 2005; Kassin et al. 2007) and are often biased by selection criteria. Despite a conspicuous number of studies that have been carried out with long-slit and IFU observations, it is still debated whether the relation and, in particular, its zero point evolves with redshift (e.g. Weiner et al. 2006; Puech et al. 2008; Dutton et al. 2011; Tiley et al. 2016) or not (e.g. Flores et al. 2006; Miller et al. 2011, 2012).

The main limitation of IFU observations of high- z galaxies is the spatial resolution. With no adaptive optics (AO), the best achievable spatial resolution is of the order of 0.5–1 arcsec imposed by the atmosphere. A galaxy at redshift $z \sim 1$ –2 with typical size of $\sim 2''$ may therefore be observed with less than 3–4 resolution elements along the whole galaxy disc. In these conditions, the point spread function (PSF) of the instrument has a strong effect on the extraction of the kinematic maps, i.e. the velocity field and velocity dispersion field, from the emission-line data cubes and on the derivation of the kinematic parameters. The so-called *beam smearing* is an issue that is well known in HI astronomy (e.g. Bosma 1978; Begeman 1987) and it causes a degeneracy between the measured rotation velocity, which ends up being underestimated, and the velocity dispersion, which can be severely overestimated, especially in the inner regions of a galaxy. In the HI community, the problem has been tackled by building artificial 3D observations that incorporate a convolution with the PSF (called beam in radioastronomy) and by comparing them with the observed data cubes (e.g. Corbelli & Schneider 1997; Lelli et al. 2014).

Recombination line observations of high- z galaxies are strongly affected by beam smearing (e.g. Davies et al. 2011; Stott et al. 2016). As a result, high- z galaxies re-observed with AO have systematically shown a shift from dispersion to rotation-dominated classification (Förster Schreiber et al. 2009; Newman et al. 2013). However, AO guarantees high spatial resolutions but at a considerable loss in term of signal-to-noise (S/N), which is not desirable for high- z low surface brightness galaxies. Moreover the larger sensitivity of natural seeing observations can reveal the fainter edges of galaxies and allows a better sampling of the flat part of the rotation curves as well as more reliable measurements of the velocity dispersion.

In this paper, we used a new 3D fitting code, called ^{3D}BAROLO¹ (Di Teodoro & Fraternali 2015), to kinematically model a sample of 18 star-forming galaxies at $z \sim 1$ observed in the H α emission line with the KMOS IFU at the VLT. This code incorporates a number of techniques that have been designed and tested in the last three decades mostly in the HI community. The originality of our approach is that we build tilted-ring galaxy models and produce a series of mock observations in the 3D observational space (two spatial and one spectral dimensions). These models are then directly fitted to observed emission-line data cube. Our method takes advantage of the full information available in data cubes and does not require any projection or extraction of kinematic maps. As a

consequence, the derived rotation velocities and velocity dispersions are not biased by beam smearing. The full procedure is described and tested in Di Teodoro & Fraternali (2015) and showed to be very powerful in recovering the true rotation curve and the intrinsic velocity dispersion, even in galaxies with 2–3 resolution elements along the major axis and S/N as low as 2–2.5 (see Sect. 4 in Di Teodoro & Fraternali 2015). Recently, another high- z -oriented code for extracting morphokinematics information of galaxies from 3D data was developed (GalPaK^{3D}; Bouché et al. 2015) and successfully tested with a few Multi Unit Spectroscopic Explorer (MUSE) observations at $z \sim 0.5$ (Bacon et al. 2015).

The paper is organized as follows. In Sect. 2 we describe the sample and selection criteria of our $z \sim 1$ disc galaxies. The kinematic modelling is discussed in Sect. 3. In Sect. 4, we show the results and we compare these results with previous kinematic studies. Section 5 recaps and discusses possible developments. In this work we assume a flat Λ CDM cosmology with $\Omega_{\text{m},0} = 0.27$, $\Omega_{\Lambda,0} = 0.73$ and $H_0 = 70 \text{ km s}^{-1} \text{ Mpc}^{-1}$. For this cosmology, $1''$ corresponds to 8.16 kpc at $z = 1$. At the same redshift, the look-back time is 7.8 Gyr. Magnitudes are always given in the AB system.

2. Data sample

Galaxies in our sample are selected from the publicly available data of the two largest high- z H α surveys carried out with the KMOS IFU at the VLT: the KMOS Redshift One Spectroscopic Survey (KROSS; Stott et al. 2016) and the KMOS^{3D} Survey (Wisnioski et al. 2015). The KROSS survey, upon completion, will have observed H α emission from about 1000 typical star-forming galaxies at $0.8 \lesssim z \lesssim 1.0$, which were selected by applying an observed magnitude cut $K_{\text{AB}} < 22.5$ and a colour cut $r - z < 1.5$ to favour blue star-forming galaxies. The KMOS^{3D} is a survey of about 600 galaxies at $0.7 \lesssim z \lesssim 2.7$ with a cut $K_s < 23$. Galaxies in KROSS and in KMOS^{3D} belong to well-studied fields of large surveys, such as the Ultra Deep Survey (UDS), the Cosmological Evolution Survey (COSMOS), and The Great Observatories Origins Deep Survey (GOODS), and have accurate spectroscopic redshifts.

We built a galaxy database from 12 KROSS pointing (COSMOS F0-F1-F2-F9-F10, ECDFS F1-F2-F3-F4-F6, and UDS F7-F16) and 6 KMOS^{3D} pointing (GS3 P1-P2, U3 P1-P2-P3, COS3 P2), for a total number of 316 galaxies. From this parent sample (we refer to Wisnioski et al. 2015; Stott et al. 2016, for the properties of the KROSS and KMOS^{3D} galaxy populations), we downselected a small subsample of galaxies based on the following criteria. We required an integrated H α flux $F_{\text{H}\alpha} > 5 \times 10^{-17} \text{ erg s}^{-1} \text{ cm}^{-2}$, such that we have an acceptable S/N and we can identify galaxy emission regions with confidence. Galaxies that have at least one catalogued source within a projected radius $\Delta r < 2''$ and a $\Delta z < 0.002 \approx 600 \text{ km s}^{-1}$ were excluded as possible merging systems. Moreover, we selected galaxies that have inclination angles in the interval $30^\circ < i < 70^\circ$. Below 30° , rotation curves become highly uncertain because of the smaller rotational component along the line of sight and the large impact of inclination errors. In addition, more inclined discs extend over a larger number of spectral channels, giving more information to constrain the models. Above $i \sim 70^\circ$, our approach could progressively underestimate rotation velocity and overestimate velocity dispersion in the inner regions of galaxies (Di Teodoro & Fraternali 2015). These criteria guarantee the highest reliability for our 3D kinematic modelling. Finally, our galaxies are selected to span over a relatively wide range in

¹ The code is publicly available at <http://editeodoro.github.io/Bbarolo>

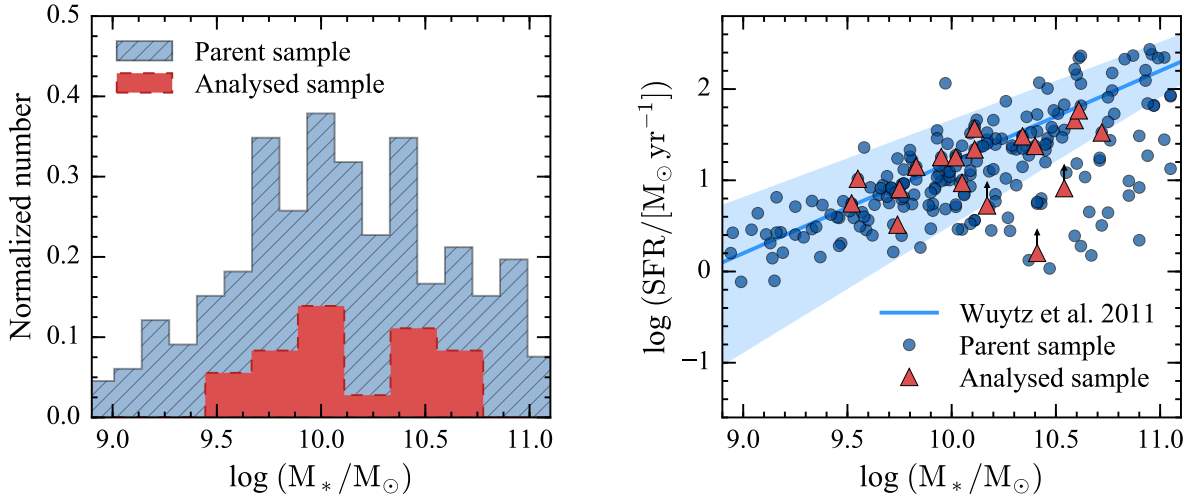


Fig. 1. *Left:* stellar-mass distribution of our final sample of 18 galaxies (red histogram) compared to that of the parent sample (cyan dashed histogram). The number of galaxies is normalized for a better visualization. *Right:* main sequence of galaxies. Blue dots represent the parent sample, and red triangles indicate our final kinematical sample. Symbols with arrows denote lower limits to SFR measures (see Sect. 2). Shaded regions indicate the 68% confidence contours of the main-sequence fit by Wuytz et al. (2011) at $0.5 < z < 1.5$.

stellar masses, from $3 \times 10^9 M_{\odot}$ to $5 \times 10^{10} M_{\odot}$. At the end, we were left with a few tens of galaxies. We visually inspected their KMOS data cubes and build a final sample of 18 galaxies by selecting those without strong skylines overlapping with the emission, more homogeneous noise across the cubes, and $H\alpha$ emission spread over more than eight channels. This last step may introduce a bias in our final sample, which is however difficult to quantify. To our understanding, none of the above criteria should systematically influence the location of our galaxies in the TFR (see also below). We note that all our selections are carried out a priori; once we decided to analyse a galaxy, it was kept in the final sample.

Our final sample includes 18 star-forming galaxies, 14 observed by KROSS, and 4 by KMOS^{3D}. Fifteen of our galaxies are included in the 3D-HST Treasury Survey (3D-HST; Brammer et al. 2012; Skelton et al. 2014). Stellar masses for galaxies in the UDS and GOODS-S fields are taken from the Cosmic Assembly Near-infrared Deep Extragalactic Legacy Survey (CANDELS; Grogin et al. 2011; Koekemoer et al. 2011) and are average values obtained by using different estimators (for details, see Santini et al. 2015). For galaxies in the COSMOS field, stellar masses are taken either from the COSMOS or 3D-HST catalogues and are derived using the Fitting and Assessment of Synthetic Templates (FAST; Kriek et al. 2009), a code that basically fits stellar population synthesis templates (Bruzual & Charlot 2003) to broadband photometry by assuming an initial mass function of Chabrier (2003). In Fig. 1 we show the stellar-mass distribution (left panel) for our sample of 18 galaxies compared to the parent sample from which they were selected. Given the exiguity of our final sample, any statistical test to match it to the parent sample would be meaningless. However, our 18 galaxies roughly follow the stellar mass distribution of the parent sample.

Star formation rates are taken from 3D-HST (Whitaker et al. 2014, estimated from IR + UV luminosities). For three of our galaxies (upwards pointing arrows in the left panel of Fig. 1), the SFR is calculated from the measured $H\alpha$ luminosities, following Kennicutt (1998) ($\text{SFR}[M_{\odot} \text{ yr}^{-1}] = 7.9 \times 10^{-42} L_{H\alpha} [\text{erg s}^{-1}]$). This latter may be read as lower limits, since no correction for the global dust extinction has been applied. Figure 1 (right panel) shows the SFR-stellar mass relation

(main sequence) for our sample of 18 galaxies compared to the parent sample. All our galaxies lie within $\pm 1\sigma$ of the main sequence at $0.5 < z < 1.5$ (Wuytz et al. 2011), except the three for which the SFRs have been calculated from the $H\alpha$ fluxes (shown as lower limits in the plot). On the whole, the SFRs of our final sample, although higher than the average SFRs of local discs, show the non-starburst nature of these galaxies.

In Fig. 2, we show rest-frame blueband images from CANDELS, $H\alpha$ total intensity maps (0th moment), and $H\alpha$ velocity fields (1st moment) extracted from the KMOS observations. The velocity fields of these galaxies reveal that these systems are regularly rotating discs. Given the range of stellar masses ($9.5 < \log(M_*/M_{\odot}) < 10.8$) and SFRs ($1 < \text{SFRs} < 50 M_{\odot} \text{ yr}^{-1}$), these systems are excellent candidates to be progenitors of local ($z = 0$) spiral galaxies (Behroozi et al. 2013). Table 1 summarizes the main properties of our galaxy sample.

Raw data were fetched from the public ESO archive and data reduction was performed using the REFLEX/ESOREX software (Freudling et al. 2013). The reduction pipeline for the KMOS instrument (Davies et al. 2013) goes through flat fielding, illumination correction, wavelength calibration, and sky subtraction (Davies et al. 2011) recipes. The final set of data includes fully reduced data cubes, raw data cubes that are not sky subtracted, and data cubes of stars observed during the pointing of scientific targets.

3. Kinematic modelling

We modelled the kinematics of the galaxies in our sample with the 3D code ^{3D}BAROLO (Di Teodoro & Fraternali 2015). This software builds tilted-ring models and compares them directly in the 3D observational space. The model is described by three geometrical parameters, i.e. the coordinates of the galaxy centre (x_0, y_0), the inclination i , and the position angle ϕ , and three kinematic parameters, i.e. the redshift z , the rotation velocity V_{rot} , and the velocity dispersion of the warm gas $\sigma_{H\alpha}$. Our approach consists of estimating these quantities in annuli of increasing distance from the galaxy centre without making any a priori assumption on their trend with radius.

The main advantage of modelling the 3D data cubes instead of the 2D maps is that the instrumental and atmospheric effects,

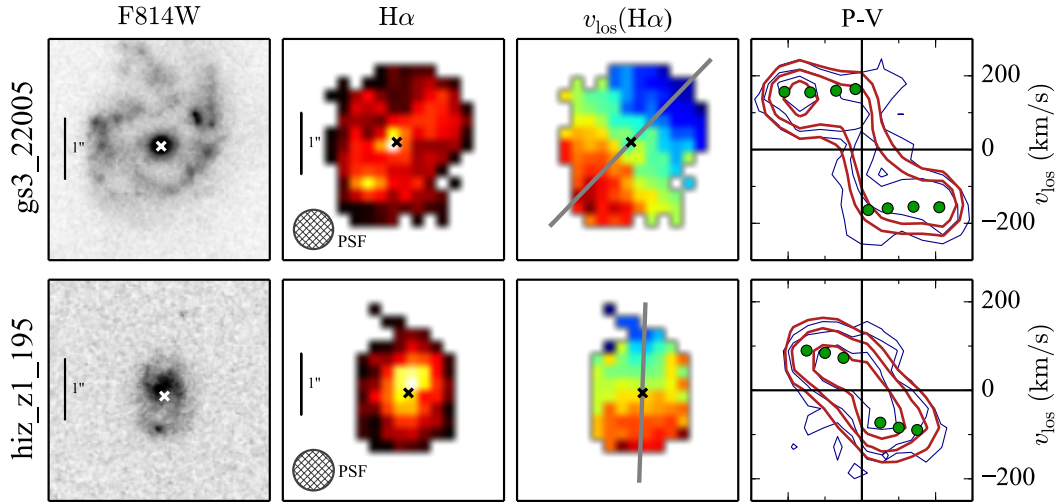


Fig. 2. Examples of two galaxies, *zcos_z1_202* and *zmus_z1_125*, used in this work. *From the left to the right:* HST images in the *F814W* filter (roughly corresponding to *I*) from the CANDELS survey, total $H\alpha$ intensity maps, $H\alpha$ velocity fields, and the comparison between model and data through position-velocity diagrams (P-Vs) taken along the kinematic major axis. Moment maps and P-Vs are extracted from the KMOS data cubes used in this paper. For the maps: white and black crosses are the adopted centres, the grey thick line is the adopted kinematic position angle. Empty circles denote the PSFs. For the P-Vs: the x -axis represents the offset along the major axis from the galaxy centre, the y -axis the line-of-sight velocity in km s^{-1} centred at the systemic velocity of the galaxy. Data are shown as blue and grey (negatives) thin lines, our best models as thick red lines. The green dots denote the ${}^{3\text{D}}\text{BAROLO}$'s rotation velocities. An equivalent figure for the full galaxy sample is available in [Appendix A](#).

i.e. the point spread function (PSF), which determines the spatial resolution, and the line spread function (LSF), which describes the spectral broadening, are incorporated directly in the model. The average PSF for each galaxy was obtained by 2D Gaussian fits of the three stars observed in each pointing. Since the observations were carried out in natural seeing mode, the typical spatial resolution is $FWHM \sim 0.6''\text{--}0.8''$. The spectral broadening is derived through a Gaussian fit of the hydroxyl (OH) sky emission lines in the data cubes that are not sky subtracted at wavelengths close to the $H\alpha$ emission of each galaxy. The resulting LSFs have typically variance $\sigma_{\text{instr}} \sim 25\text{--}30 \text{ km s}^{-1}$.

The modelling with ${}^{3\text{D}}\text{BAROLO}$ requires the initial estimate of the coordinates of the centre, the inclination, and the position angles. We use publicly available *Hubble* Space Telescope (HST) images from the CANDELS survey (Fig. 2, leftmost panels) to determine the centres of the galaxies. The inclination angles are estimated both through an elliptical fit to the isophotes of the HST images (i_{opt}) and through the fitting of a PSF-convoluted disc model to the total $H\alpha$ intensity maps ($i_{H\alpha}$). We assume infinitely thin discs, since the effect of the spatial resolution (about 5 kpc) dominates over any realistic intrinsic galaxy thickness. Several tests on mock galaxies showed that the latter method ($i_{H\alpha}$) can recover the true inclination with errors lower than 5 degrees in the range $30^\circ < i < 70^\circ$, regardless of the spatial resolution (Di Teodoro & Fraternali 2015). We use the average value between i_{opt} and $i_{H\alpha}$ as fiducial inclination angle, but the full range of possible inclinations is taken into account in the estimate of errors on the kinematic quantities. Velocity fields, derived through Gaussian fits to the line profiles, are used to infer the kinematic position angles. Adopted centres and position angles are shown in Fig. 2 as crosses and grey thick lines, respectively. Accurate spectroscopic redshifts are taken from the 3D-HST and COSMOS catalogues and are used as the spectral centre for the $H\alpha$ emission line.

The galaxy emission regions in each channel map of the data cubes is identified by taking only pixels with fluxes larger than $1.5\text{--}2.5 \sigma_{\text{noise}}$, depending on the reduction quality of the data cubes, where σ_{noise} is the spread of the noise distribution.

Since the noise between the channel maps is not constant and does not follow a Gaussian distribution, we estimate the noise statistics using only pixels with negative values, which instead are fairly distributed as Gaussian functions centred on zero. We calculate σ_{noise} by fitting Gaussian functions to the negative noise distribution and build the mask of regions with $F > 1.5\text{--}2.5 \sigma_{\text{noise}}$ channel by channel, so that each channel has a different noise. Such a mask identifies the pixels that are considered as genuine galaxy emission by the ${}^{3\text{D}}\text{BAROLO}$ fitting algorithm. All masks were visually inspected and checked to guarantee that residual contamination from skylines does not invalidate the successive kinematic modelling.

The surface brightness of galaxies is not fitted, but models are locally normalized to the velocity-integrated $H\alpha$ flux pixel by pixel. Since the number of pixels that can be used to constrain the model is very small in these high- z data cubes, we decided to keep the geometrical parameters fixed and fit only the rotation velocity and intrinsic velocity dispersion of the gas. The uncertainties on the geometrical parameters however are propagated in the errors on the rotation velocity and velocity dispersion. Errors on V_{rot} and $\sigma_{H\alpha}$ are estimated by using a Monte Carlo sampling of the full parameter space in the region close to the minimum as described in Di Teodoro & Fraternali (2015). The errors in the flat rotation velocity resulting from this procedure typically correspond to uncertainties in the inclinations of about 5 degrees, which is, on average, the difference that we have between i_{opt} and $i_{H\alpha}$. However, in five galaxies (1, 7, 9, 10, 11) we noticed that this difference is appreciably larger and thus we revised their velocity errors by assuming an inclination uncertainty of 10 degrees (see Table 1).

4. Results

The comparison between our best 3D models and the data is shown in Figs. 2 and A.1 (rightmost column) through position-velocity slices (P-Vs) taken along the major axis. As an example, in Fig. 3 we also show the comparison between the data cube and the best-fit model cube in five channel maps at different

Table 1. Sample of 18 disc galaxies at $z \sim 1$ analysed in this work.

#	Name	Field	RA (J2000) h m s	Dec (J2000) ° ' "	z	$\text{Log } M_*/M_\odot$	SFR M_\odot/yr	i °	V_{flat} km s^{-1}	$\langle \sigma_{\text{H}\alpha} \rangle$ km s^{-1}
(1)	(2)	(3)	(4)	(5)	(6)	(7)	(8)	(9)	(10)	
1	gs3_22005 [†]	GOODS-S	03 32 29.85	−27 45 20.5	0.954	10.72 ± 0.12	33.4	47	215 ⁺³⁰ _{−16}	30 ± 6
2	hiz_z1_195	COSMOS	10 00 34.63	+02 14 29.5	0.856	9.75 ± 0.09	8.0	49	117 ⁺¹⁶ _{−15}	26 ± 5
3	hiz_z1_258	COSMOS	10 01 05.65	+01 52 57.6	0.838	10.41 ± 0.11	1.6 ¹	54	173 ⁺²⁰ _{−18}	19 ± 7
4	u3_5138 [†]	UDS	02 16 59.89	−05 15 07.6	0.809	9.74 ± 0.12	3.3	62	128 ⁺¹⁴ _{−14}	26 ± 6
5	u3_14150 [†]	UDS	02 16 58.00	−05 12 42.6	0.896	10.11 ± 0.14	21.8	50	144 ⁺¹⁵ _{−15}	27 ± 5
6	u3_25160 [†]	UDS	02 17 04.69	−05 09 46.4	0.897	10.05 ± 0.15	9.3	53	133 ⁺¹³ _{−13}	23 ± 3
7	zcos_z1_192	COSMOS	10 01 03.45	+01 54 00.4	0.917	10.17 ± 0.05	5.3 ¹	45	147 ⁺²⁷ _{−15}	35 ± 5
8	zcos_z1_202	COSMOS	10 00 53.39	+01 52 40.8	0.841	10.54 ± 0.06	8.2 ¹	45	188 ⁺¹⁷ _{−13}	39 ± 6
9	zcos_z1_690	COSMOS	10 00 36.54	+02 13 09.5	0.927	10.59 ± 0.25	45.6	50	208 ⁺²⁶ _{−16}	38 ± 6
10	zcos_z1_692	COSMOS	10 00 36.42	+02 11 19.2	0.930	10.61 ± 0.18	58.4	42	190 ⁺³⁸ _{−25}	22 ± 5
11	zmus_z1_21	GOODS-S	03 32 48.48	−27 54 16.0	0.839	10.40 ± 0.14	23.8	32	157 ⁺⁴⁶ _{−31}	25 ± 4
12	zmus_z1_86	GOODS-S	03 32 25.19	−27 51 00.1	0.841	9.55 ± 0.08	10.3	51	109 ⁺¹³ _{−11}	24 ± 4
13	zmus_z1_119	GOODS-S	03 32 08.20	−27 47 52.1	0.840	10.34 ± 0.07	30.3	62	179 ⁺¹⁵ _{−15}	31 ± 6
14	zmus_z1_125	GOODS-S	03 32 21.76	−27 47 24.6	0.998	9.95 ± 0.06	17.8	58	141 ⁺¹⁴ _{−14}	36 ± 7
15	zmus_z1_129	GOODS-S	03 32 21.76	−27 47 24.6	0.995	9.83 ± 0.07	14.2	34	122 ⁺²⁶ _{−23}	38 ± 6
16	zmus_z1_166	GOODS-S	03 32 16.49	−27 44 49.1	0.975	10.11 ± 0.15	36.9	51	148 ⁺¹⁴ _{−14}	39 ± 6
17	zmus_z1_217	GOODS-S	03 32 20.51	−27 40 58.9	0.895	10.02 ± 0.08	17.9	70	146 ⁺¹² _{−12}	21 ± 4
18	zmvvd_z1_87	GOODS-S	03 32 05.66	−27 47 49.1	0.896	9.52 ± 0.08	5.6	52	96 ⁺¹¹ _{−10}	24 ± 4

Notes. (1) Name adopted in the main survey (KROSS or KMOS^{3D}); (2) field; (3)–(4) celestial coordinates in J2000; (5) spectroscopic redshift; (6) stellar masses from CANDELS (Santini et al. 2015) or COSMOS/3D-HST (see text); (7) star formation rates from 3D-HST (Whitaker et al. 2014, $SFR_{\text{UV}} + SFR_{\text{IR}}$) or derived from integrated H α flux (lower limits); (8) estimated inclination angle; (9) velocity of the flat part of the rotation curve, defined as specified in Sect. 4, derived in this work; (10) intrinsic H α velocity dispersion averaged over the entire galaxy disc as derived in this work. ^(†) Galaxies belonging to the KMOS^{3D} survey. Unmarked galaxies belong to the KROSS survey. ⁽¹⁾ SFR from H α integrated flux (Kennicutt 1998).

velocities for the galaxies zcos_z1_202 and zmus_z1_125. In both Figs. 2 and 3, blue thin contours represent the data and red thick contours the models. The models satisfactorily reproduce the data and, in particular, the P-Vs show that the lowest contours are well traced in most cases. These contours are very sensitive to the actual rotation velocities, testifying to a well-attained fit. The density asymmetries between the approaching and receding sides in our models are due to the pixel-to-pixel normalization, whereas the kinematics is always assumed axisymmetric. Figure 4 shows the derived rotation curves (top panels) and intrinsic velocity dispersions (bottom panels) for galaxies with $\log(M_*/M_\odot) < 10.1$ (left panels) and $\log(M_*/M_\odot) > 10.1$ (right panels).

The rotation curves of our galaxy sample are remarkably flat, in most cases from the first to last measured point. We stress that, unlike previous kinematic studies at high redshifts (e.g. Puech et al. 2008; Epinat et al. 2009; Swinbank et al. 2012; Bacon et al. 2015; Wuyts et al. 2016), we do not assume a parametric form for the kinematic quantities. In particular, we do not force the rotation curves to follow any functional form (e.g. $V_{\text{rot}}(R) \propto \arctan(R)$), but at each radius the velocity is estimated independently. The inner velocity points of most galaxies are already in the flat part of the rotation curves, implying that the velocity rises very steeply in the inner few kiloparsecs. Overall,

the shape of the rotation curves of these $z \sim 1$ galaxies is akin to that of discs in the local Universe with similar stellar mass (e.g. Persic & Salucci 1991; Casertano & van Gorkom 1991). Similar to local spiral galaxies, the dynamics of these high- z systems is supposed to be dominated by the baryonic matter in the inner regions and by the dark matter halo in the outer regions (Begeman 1987; Persic et al. 1996). Observations of damped Lyman α absorbers (DLAs) show that the fraction of neutral gas in galaxies does not significantly evolve with redshift (e.g. Zafar et al. 2013) and, consistently with local disc galaxies, we can assume $M_{\text{HI}} \simeq 0.1\text{--}0.2 M_*$ (e.g. Papastergis et al. 2012). Instead, CO observations suggest that the molecular gas fraction at $z \sim 1$ is about three times higher than in the local Universe (e.g. Tacconi et al. 2010), leading to $M_{\text{H}_2} \simeq 0.4 M_*$. The comparison between the total baryonic mass $M_* + M_{\text{gas}}$, where $M_{\text{gas}} = M_{\text{HI}} + M_{\text{H}_2} \sim 0.5\text{--}0.6 M_*$, and the dynamical mass $M_{\text{dyn}} = R_{\text{last}} V_{\text{rot}}^2(R_{\text{last}})/G$ enclosed within the last measured radius R_{last} suggests that these galaxies must have dark matter fractions of 30–50% of the total mass.

In order to place our galaxies on the stellar mass Tully-Fisher relation, we calculated the circular velocity V_{flat} of the flat part of the rotation curves as the average velocity over the rings with the innermost point excluded. The resulting V_{flat} for each galaxy are listed in Table 1, Col. 8. Adopted stellar masses are

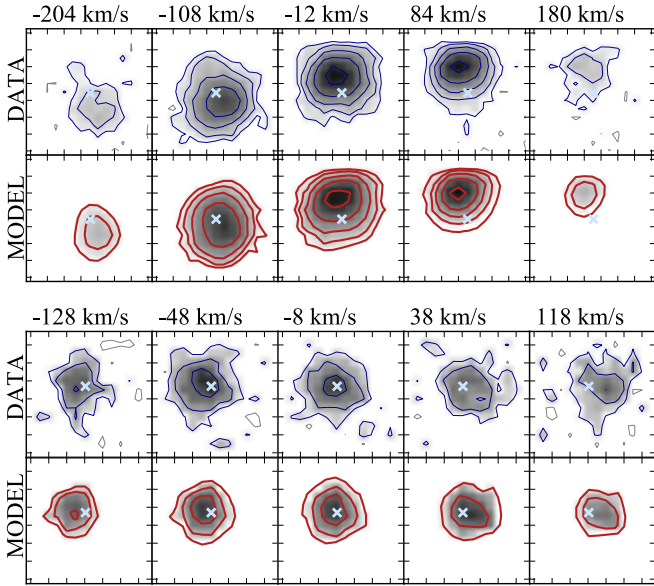


Fig. 3. Comparison between the KMOS data cubes (thin blue contours, upper panels) and the ^{3D}BAROLO best-fit model-cubes (thick red contours, lower panels) for the high-mass galaxy *zcos_z1_202* at $z = 0.84$ (top) and the low-mass galaxy *zmus_z1_125* at $z = 0.99$ (bottom). Negative contours are shown as thin grey lines in the data. Cyan crosses represent the centre of the galaxies. We show five representative channel maps: the *central panels* represent the channel closest to the systemic velocity of the galaxy, the *rightmost and leftmost panels* indicate the extreme velocities, and the *second and fourth panels* indicate the intermediate velocities. Boxes have sizes of about $3'' \times 3''$, the PSFs are $0.72''$ for *zcos_z1_202* and $0.79''$ for *zmus_z1_125*.

listed in Table 1, Col. 6. Figure 5 shows the Tully-Fisher relation for our sample of galaxies, shown as red circles, compared to previous studies. We fitted our data points to the TFR in the form $\log(M_*) = a + b \log(V_{\text{flat}})$ using the orthogonal distance regression technique to take errors in the ordinate and abscissa into account. Our best fit has a zero-point $a = 1.88 \pm 0.46$ and a slope $b = 3.80 \pm 0.21$ and it is shown as a thick-shadowed red line in Fig. 5. For comparison, we also show the best fit for the local ($z < 0.1$) Tully-Fisher relation derived by Reyes et al. (2011) (green dash-dotted line). Our best-fit relation is consistent with this local relation.

We tested the effect of uncertainties in the inclination angles of our galaxies on the TFR. Inclination angles (i) are very important in the determination of the rotation velocities, which is mostly because the measured (l.o.s. projected) velocities are corrected by $\sin(i)^{-1}$ to obtain the intrinsic rotations (see Table 1). If a galaxy is intrinsically at $i > 50^\circ$ but our estimate of inclination is wrong by 10 degrees, the errors in the derived velocities are contained to $< 10\%$. However for more face-on galaxies (for which the inclination is even more difficult to estimate) an error can have dramatic consequences. If a galaxy is at $i = 30$ but we estimate $i = 20$ ($i = 40$), its velocity would be off by 46% (22%). In order to test the effect of potential errors in our inclinations, we split our sample in two considering the nine galaxies having $i > 50^\circ$ and those with $i \leq 50^\circ$, shown with different symbols in Fig. 5. There is a slight offset between the two samples perhaps hinting at some underestimation of inclination correction for lowly inclined galaxies. If we fit the TFR only to the points above $i > 50^\circ$, we obtain $a = 2.33 \pm 0.49$ and a slope

$b = 3.60 \pm 0.25$. On the whole, our analysis supports the idea of a not evolving or weakly evolving TF relation as found, for example by Miller et al. (2011, 2012) rather than an evolving relation (e.g. Kassin et al. 2007; Dutton et al. 2011).

Recently, a Tully-Fisher relation from the KROSS team was published (Tiley et al. 2016). These authors used a sample of 56 galaxies that were selected to have $V/\sigma > 3$ from a much larger sample. This selection was carried out a posteriori, unlike ours. They find evidence for a significant evolution of the zero point of the stellar-mass TFR. A possible reason for the difference between our results and theirs is the different way we estimated inclination angles. They derived inclinations from the fitting of velocity fields and this may give systematically lower values than our method.

Velocity dispersions (Fig. 4, bottom panel) show no unique trend with radius, although the dispersion profiles appear roughly flat on average. The derived values of dispersions are between 15 and about 40 km s^{-1} , even in the regions close to the galaxy centres. These values are fully comparable to $\text{H}\alpha$ velocity dispersions measured in disc galaxies in the local Universe (e.g. Andersen et al. 2006; Bershady et al. 2010; Epinat et al. 2010). Following Wisnioski et al. (2015), we show in Fig. 6 the evolution with redshifts of velocity dispersion derived in previous kinematic studies of the warm medium. The plot includes both studies carried out with IFU observations, i.e. GHASP (Epinat et al. 2010), DYNAMO (Green et al. 2014), KMOS^{3D} (Wisnioski et al. 2015), MASSIV (Epinat et al. 2012; Vergani et al. 2012), SINS/zC-SINF (Förster Schreiber et al. 2009), OSIRIS (Law et al. 2007, 2009), and AMAZE-LSD (Gnerucci et al. 2011) surveys, and with long-slit observations, i.e. DEEP2 survey (Kassin et al. 2012). All the above-mentioned studies were based on the $\text{H}\alpha$ emission line, but we stress that they used different instruments and different estimators to derive the gas velocity dispersion. The average velocity dispersions $\langle \sigma_{\text{H}\alpha} \rangle$ derived in this work (Table 1, Col. 9) for each galaxy are shown as large red circles.

The dispersions derived by our 3D approach are similar to the results found by Wisnioski et al. (2015) (grey circles) using a larger sample of galaxies observed with KMOS, but overall smaller than the values quoted in the majority of previous works at similar redshifts (e.g. Epinat et al. 2012; Kassin et al. 2012). However the values quoted by Wisnioski et al. (2015) are measured from the outermost regions and along the major axis of the galaxies in the velocity dispersion maps, where the effect of beam smearing is less significant (Förster Schreiber et al. 2009) and do not provide information about the intrinsic dispersion in the inner regions of the galaxies. Instead, our values in Fig. 6 are intrinsic velocity dispersions averaged over the whole galaxy disc. The fact that our average values are consistent with those measured in regions where the beam smearing effect is negligible confirms the ability of ^{3D}BAROLO to correct for instrumental broadening of the emission line.

The mean value over our whole sample is $\sim 29 \text{ km s}^{-1}$, showing that there has been hardly any evolution in the velocity dispersion in the last ~ 8 Gyr. In other words, these discs were not more turbulent and/or dynamically hotter than the local discs. Finally, another important parameter is the V/σ ratio, which measures the relative importance of ordered (V) and random (σ) motions in the dynamical support of a galaxy. Systems in our sample have $V/\sigma_{\text{H}\alpha}$ in the range 3–10, suggesting that these discs with normal SFRs are already fully settled and rotational supported at $z \sim 1$.

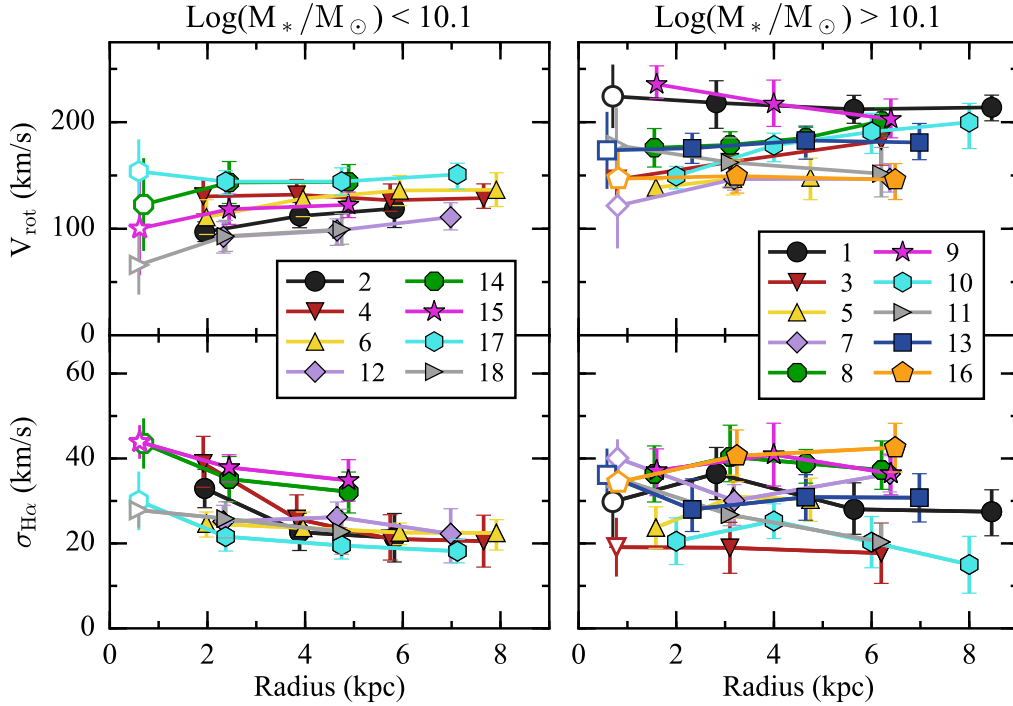


Fig. 4. Rotation curves (*top*) and velocity dispersions (*bottom*) derived by fitting 3D tilted-ring models to H α data cubes of our galaxy sample with ^{3D}BAROLO. *Left panels* refer to galaxies with $\log(M_*/M_\odot) < 10.1$; *right panels* to galaxies with $\log(M_*/M_\odot) > 10.1$. Empty data points indicate uncertain measurements in the inner regions of galaxies. For these points, we assumed the derived velocity dispersion as the error for the rotation velocity. Galaxies are numbered as in Fig. 1. Radii are slightly oversampled (about 2 rings per resolution element). Rotation curves are remarkably flat from the first to the last point; velocity dispersion are lower than $\sim 40 \text{ km s}^{-1}$.

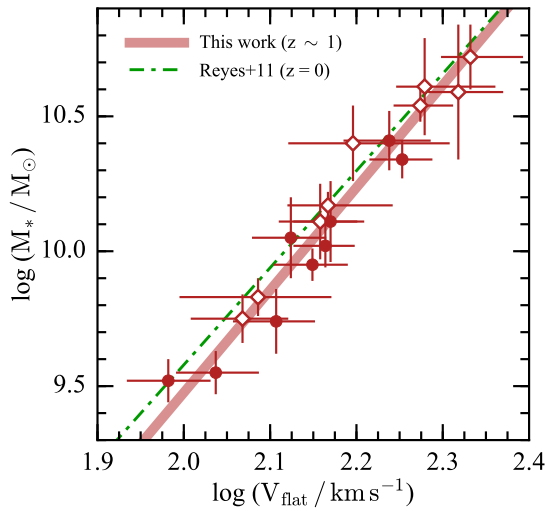


Fig. 5. Stellar mass Tully-Fisher relation derived for our 18 galaxies (red circles) in the redshift interval $0.84 \lesssim z \lesssim 1$. Full circles represent galaxies with $i > 50$; empty diamonds are galaxies with $i \leq 50$. Lines are the fit of the relation $\log(M_*) = a + b \log(V)$. The thick red line is the best fit to our full data sample, $a = 1.88$, $b = 3.80$. Green dash-dotted line is the local TFR by Reyes et al. (2011) for $z < 0.1$ ($a = 2.39$, $b = 3.59$). Our points are compatible with no strong evolution of the relation.

5. Concluding remarks

In this paper we applied, for the first time, a new 3D modelling software (^{3D}BAROLO) to H α emission-line data cubes of a sample of 18 star-forming galaxies at $z = 0.85$ – 1 observed with the KMOS IFU. The low spatial resolution of these

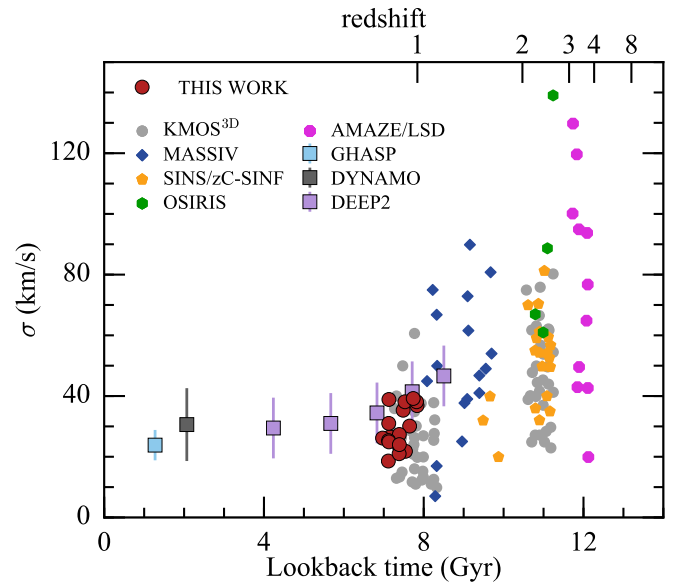


Fig. 6. Evolution of gas velocity dispersion throughout the cosmic time. Data are taken from different studies on star-forming galaxies observed in the surveys coded in the legend. For $z \lesssim 1$, average values over large galaxy samples are shown as squares. Other symbols indicate measurements in single galaxies. The average velocity dispersion derived in this work are shown as red circles. Our values are compatible with no evolution from $z \sim 1$ to now.

observations makes it difficult to derive the intrinsic kinematics of high- z galaxies using traditional 2D techniques. In particular, kinematic maps are strongly affected by beam smearing with a

consequent overestimation of dispersion velocities and the underestimation of rotation velocities. Our software aims to overcome these problems by building models of mock galaxies with different parameters and fitting them directly to the 3D emission contained in the data cubes. This is the same procedure used in GalPaK^{3D} (Bouché et al. 2015) for high- z or TiRiFiC for low- z galaxies (Józsa et al. 2007). However, GalPaK^{3D} uses parametric functions for the trend of the various physical properties in particular the rotation velocity, whereas we derive the actual value of the velocity at every galactic radius.

To our knowledge, all other techniques applied to high- z galaxies work in 2D with the exception of DYSMAL (Cresci et al. 2009). This software builds a 3D mock observation of the galaxy but, unlike our code, performs the fit of the data in 2D via the extraction of velocity maps. Other 2D (or 1D) techniques employ beam smearing corrections using different methods (see e.g. the description in Stott et al. 2016, Appendix A). Davies et al. (2011), comparing different techniques, concluded that only methods employing a 3D deconvolution do not have residual beam smearing effects in the estimates of velocity dispersions. Working in 2D has the obvious advantage that it is faster than 3D and is applicable to data with relatively low S/N. Thus, large data samples can be analysed with 2D techniques.

In this paper we have taken a different approach and concentrated on a small sample of 18 star-forming galaxies at $z \sim 1$ and derived their rotation curves and intrinsic velocity dispersions. Our analysis revealed that the kinematics of our sample of high- z galaxies is comparable to that of local disc galaxies with steeply rising rotation curves (within few kiloparsecs) followed by a flat part. We measured low intrinsic H α velocity dispersions ($\sigma_{\text{H}\alpha} \sim 15\text{--}40 \text{ km s}^{-1}$) over the entire disc, revealing that turbulence plays a similar role in these systems as in nearby galaxies, despite their somewhat larger SFRs. Baryonic matter contributes roughly 50%–70% the dynamical mass in the disc regions probed by our data. In addition, these galaxies appear to lie on the local stellar-mass Tully-Fisher relation. All our findings suggest that disc galaxies were already dynamically mature about 8 Gyr ago.

Acknowledgements. We thank G. Zamorani for useful discussions. This study is based on public data selected from the KROSS (ESO IDs: 092.B-0538(B), 092.D-0511(B), 0.93.B-0106(A), 094.B-0061(C)) and the KMOS^{3D} (ESO ID: 092.A-0091(C)) surveys. Data were obtained from the ESO Science Archive Facility and were reduced by using ESO software and pipelines. This research has made use of the HST-COSMOS, 3D-HST, and CANDELS databases. E.d.T. and F.F. acknowledge financial support from PRIN MIUR 2010-2011, project “The Chemical and Dynamical Evolution of the Milky Way and Local Group Galaxies”, prot. 2010LY5N2T.

References

- Andersen, D. R., Bershady, M. A., Sparke, L. S., et al. 2006, *ApJS*, 166, 505
 Bacon, R., Brinchmann, J., Richard, J., et al. 2015, *A&A*, 575, A75
 Begeman, K. G. 1987, Ph.D. Thesis, Groningen Univ.
 Behroozi, P. S., Wechsler, R. H., & Conroy, C. 2013, *ApJ*, 770, 57
 Bell, E. F., & de Jong, R. S. 2001, *ApJ*, 550, 212
 Bershady, M. A., Verheijen, M. A. W., Swaters, R. A., et al. 2010, *ApJ*, 716, 198
 Bosma, A. 1978, Ph.D. Thesis, Groningen Univ.
 Bouché, N., Carfantan, H., Schroetter, I., Michel-Dansac, L., & Contini, T. 2015, *AJ*, 150, 92
 Brammer, G. B., van Dokkum, P. G., Franx, M., et al. 2012, *ApJS*, 200, 13
 Bruzual, G., & Charlot, S. 2003, *MNRAS*, 344, 1000
 Casertano, S., & van Gorkom, J. H. 1991, *AJ*, 101, 1231
 Chabrier, G. 2003, *PASP*, 115, 763
 Conselice, C. J., Bundy, K., Ellis, R. S., et al. 2005, *ApJ*, 628, 160
 Contini, T., Garilli, B., Le Fèvre, O., et al. 2012, *A&A*, 539, A91
 Corbelli, E., & Schneider, S. E. 1997, *ApJ*, 479, 244
 Cresci, G., Hicks, E. K. S., Genzel, R., et al. 2009, *ApJ*, 697, 115
 Davies, R., Förster Schreiber, N. M., Cresci, G., et al. 2011, *ApJ*, 741, 69
 Davies, R. I., Agudo Berbel, A., Wierzorrek, E., et al. 2013, *A&A*, 558, A56
 Dekel, A., Sari, R., & Ceverino, D. 2009, *ApJ*, 703, 785
 Di Teodoro, E. M., & Fraternali, F. 2015, *MNRAS*, 451, 3021
 Dutton, A. A., van den Bosch, F. C., & Dekel, A. 2010, *MNRAS*, 405, 1690
 Dutton, A. A., van den Bosch, F. C., Faber, S. M., et al. 2011, *MNRAS*, 410, 1660
 Eisenhauer, F., Abuter, R., Bickert, K., et al. 2003, in Instrument Design and Performance for Optical/Infrared Ground-based Telescopes, eds. M. Iye, & A. F. M. Moorwood, *SPIE Conf. Ser.*, 4841, 1548
 Elbaz, D., Dickinson, M., Hwang, H. S., et al. 2011, *A&A*, 533, A119
 Epinat, B., Contini, T., Le Fèvre, O., et al. 2009, *A&A*, 504, 789
 Epinat, B., Amram, P., Balkowski, C., & Marcelin, M. 2010, *MNRAS*, 401, 2113
 Epinat, B., Tasca, L., Amram, P., et al. 2012, *A&A*, 539, A92
 Flores, H., Hammer, F., Puech, M., Amram, P., & Balkowski, C. 2006, *A&A*, 455, 107
 Förster Schreiber, N. M., Genzel, R., Lehnert, M. D., et al. 2006, *ApJ*, 645, 1062
 Förster Schreiber, N. M., Genzel, R., Bouché, N., et al. 2009, *ApJ*, 706, 1364
 Freudling, W., Romaniello, M., Bramich, D. M., et al. 2013, *A&A*, 559, A96
 Genzel, R., Tacconi, L. J., Eisenhauer, F., et al. 2006, *Nature*, 442, 786
 Genzel, R., Burkert, A., Bouché, N., et al. 2008, *ApJ*, 687, 59
 Glazebrook, K. 2013, *PASA*, 30, 56
 Gnerucci, A., Marconi, A., Cresci, G., et al. 2011, *A&A*, 528, A88
 Green, A. W., Glazebrook, K., McGregor, P. J., et al. 2014, *MNRAS*, 437, 1070
 Grogin, N. A., Kocevski, D. D., Faber, S. M., et al. 2011, *ApJS*, 197, 35
 Józsa, G. I. G., Kenn, F., Klein, U., & Oosterloo, T. A. 2007, *A&A*, 468, 731
 Kassir, S. A., Weiner, B. J., Faber, S. M., et al. 2013, *A&A*, 559, A96
 Kassir, S. A., Weiner, B. J., Faber, S. M., et al. 2012, *ApJ*, 758, 106
 Kennicutt, Jr., R. C. 1998, *ARA&A*, 36, 189
 Koekemoer, A. M., Faber, S. M., Ferguson, H. C., et al. 2011, *ApJS*, 197, 36
 Kriek, M., van Dokkum, P. G., Labbé, I., et al. 2009, *ApJ*, 700, 221
 Larkin, J., Barczys, M., Krabbe, A., et al. 2006, in *SPIE Conf. Ser.*, 6269, 1
 Law, D. R., Steidel, C. C., Erb, D. K., et al. 2007, *ApJ*, 669, 929
 Law, D. R., Steidel, C. C., Erb, D. K., et al. 2009, *ApJ*, 697, 2057
 Lelli, F., Verheijen, M., & Fraternali, F. 2014, *A&A*, 566, A71
 Lilly, S. J., Carollo, C. M., Pipino, A., Renzini, A., & Peng, Y. 2013, *ApJ*, 772, 119
 McGaugh, S. S. 2005, *ApJ*, 632, 859
 Meyer, M. J., Zwaan, M. A., Webster, R. L., Schneider, S., & Staveley-Smith, L. 2008, *MNRAS*, 391, 1712
 Miller, S. H., Bundy, K., Sullivan, M., Ellis, R. S., & Treu, T. 2011, *ApJ*, 741, 115
 Miller, S. H., Ellis, R. S., Sullivan, M., et al. 2012, *ApJ*, 753, 74
 Newman, S. F., Genzel, R., Förster Schreiber, N. M., et al. 2013, *ApJ*, 767, 104
 Papastergis, E., Cattaneo, A., Huang, S., Giovanelli, R., & Haynes, M. P. 2012, *ApJ*, 759, 138
 Persic, M., & Salucci, P. 1991, *ApJ*, 368, 60
 Persic, M., Salucci, P., & Stel, F. 1996, *MNRAS*, 281, 27
 Puech, M., Flores, H., Hammer, F., et al. 2008, *A&A*, 484, 173
 Reyes, R., Mandelbaum, R., Gunn, J. E., Pizagno, J., & Lackner, C. N. 2011, *MNRAS*, 417, 2347
 Rodighiero, G., Daddi, E., Baronchelli, I., et al. 2011, *ApJ*, 739, L40
 Santini, P., Ferguson, H. C., Fontana, A., et al. 2015, *ApJ*, 801, 97
 Sharples, R., Bender, R., Agudo Berbel, A., et al. 2013, *The Messenger*, 151, 21
 Skelton, R. E., Whitaker, K. E., Momcheva, I. G., et al. 2014, *ApJS*, 214, 24
 Speagle, J. S., Steinhardt, C. L., Capak, P. L., & Silverman, J. D. 2014, *ApJS*, 214, 15
 Stott, J. P., Swinbank, A. M., Johnson, H. L., et al. 2016, *MNRAS*, 457, 1888
 Swinbank, A. M., Sobral, D., Smail, I., et al. 2012, *MNRAS*, 426, 935
 Tacchella, S., Lang, P., Carollo, C. M., et al. 2015, *ApJ*, 802, 101
 Tacconi, L. J., Genzel, R., Neri, R., et al. 2010, *Nature*, 463, 781
 Tiley, A. L., Stott, J. P., Swinbank, A. M., et al. 2016, *MNRAS*, 460, 103
 Tully, R. B., & Fisher, J. R. 1977, *A&A*, 54, 661
 Vergani, D., Epinat, B., Contini, T., et al. 2012, *A&A*, 546, A118
 Weiner, B. J., Willmer, C. N. A., Faber, S. M., et al. 2006, *ApJ*, 653, 1049
 Whitaker, K. E., van Dokkum, P. G., Brammer, G., & Franx, M. 2012, *ApJ*, 754, L29
 Whitaker, K. E., Franx, M., Leja, J., et al. 2014, *ApJ*, 795, 104
 Wisnioski, E., Förster Schreiber, N. M., Wuyts, S., et al. 2015, *ApJ*, 799, 209
 Wuyts, S., Förster Schreiber, N. M., van der Wel, A., et al. 2011, *ApJ*, 742, 96
 Wuyts, S., Förster Schreiber, N. M., Wisnioski, E., et al. 2016, *ApJ*, submitted [arXiv:1603.03432]
 Zafar, T., Péroux, C., Popping, A., et al. 2013, *A&A*, 556, A141

Appendix A: Additional figure

The full galaxy sample analysed in this work is presented in Fig. A.1. From the left to the right, for each galaxy we show: (1) the HST image in the F814W band, (2) the H α intensity map, (3) the H α velocity field, (4) the position-velocity diagram (P-V) taken along the kinematic major axis. White and black crosses

on the maps denote the centres adopted in the fit, the grey thick line on the velocity field is the kinematic position angle. In the P-V diagram, we show the comparison between the data (thin blue lines, negative contours in grey) and our best model (thick red contours). The green dots denote the inclination-projected rotation curve derived in this work.

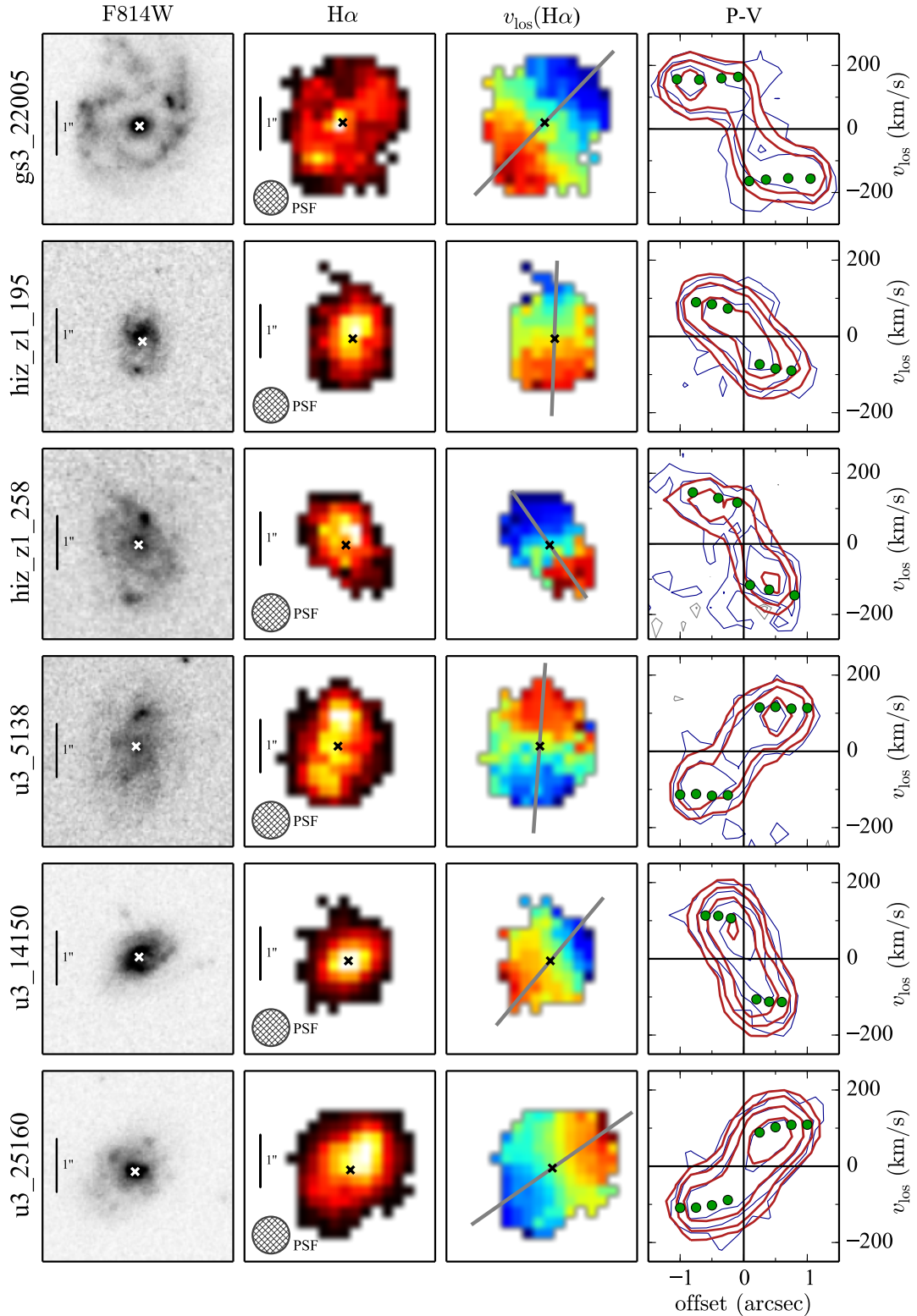


Fig. A.1. The sample of 18 galaxies used in this work.

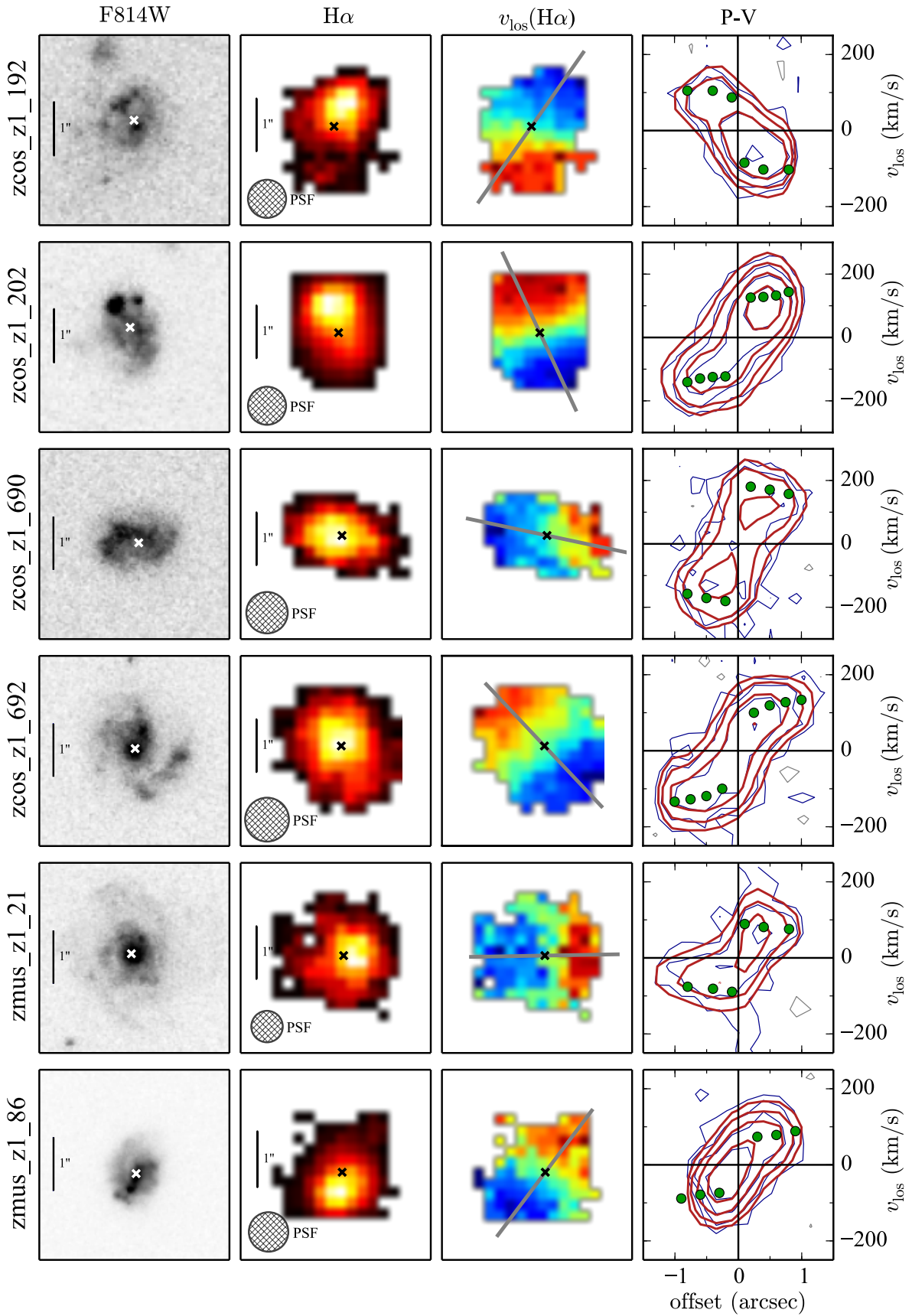


Fig. A.1. continued.

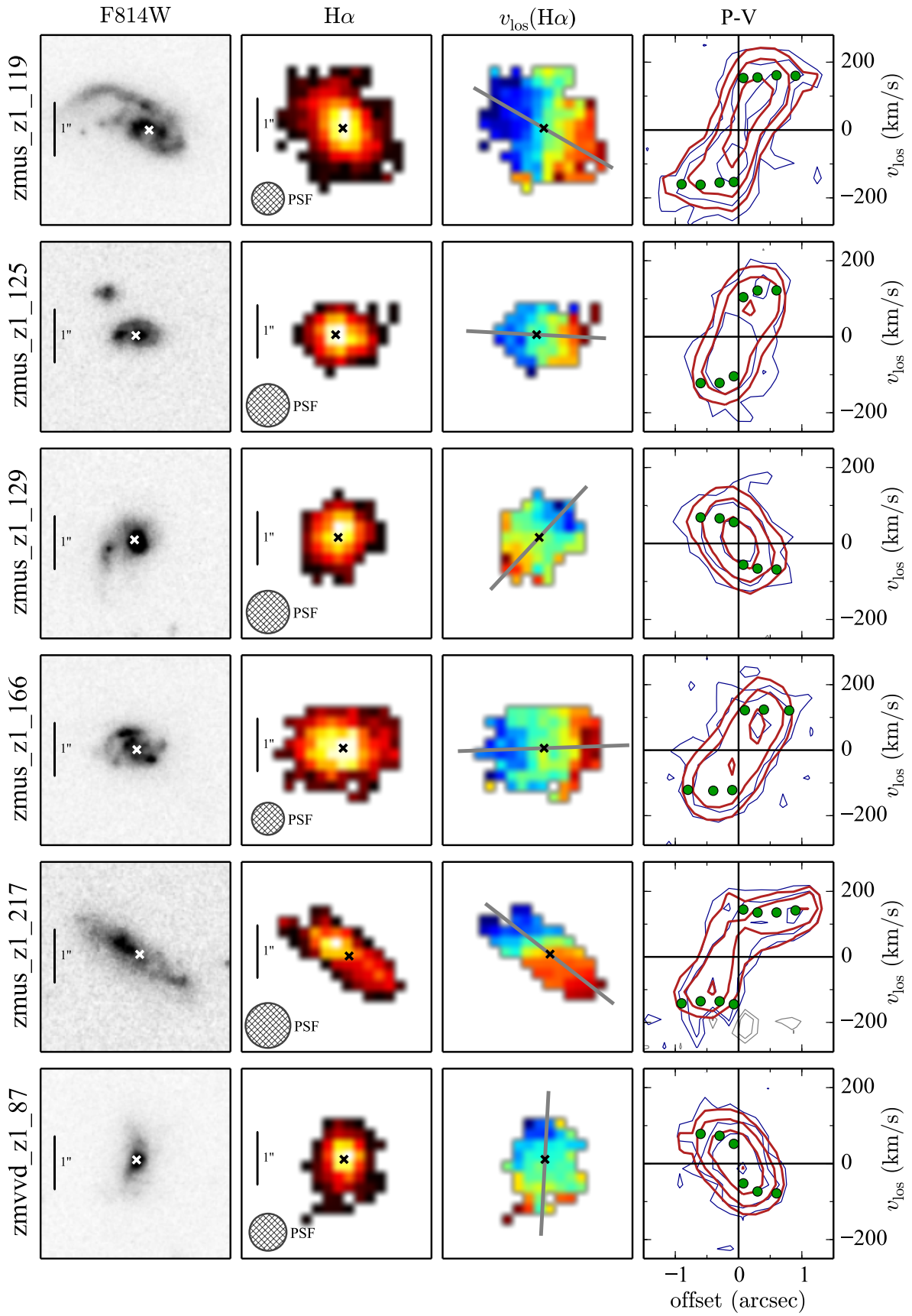


Fig. A.1. continued.